ADVANCED MATERIALS TECHNOLOGIES
www.advmattechnol.de

Fully Passive Electrochemical Oxygen Sensor Enabled With Organic Electrochemical Transistor

Lia Giulia D'Amico, Chenhong Zhang, Francesco Decataldo, Vito Vurro, Marta Tessarolo, Isacco Gualandi, Federica Mariani, Erika Scavetta, Tobias Cramer, and Beatrice Fraboni*

Wireless and battery-free sensor operation is essential for sustainable sensor networks for environmental and health monitoring. Achieving such a fully passive design in electrochemical sensors is challenging due to the need for amplification and control electronics as realized in potentiostats. To address this issue, organic electrochemical transistors (OECTs) are introduced as amplified sensors and demonstrate an OECT-based oxygen sensor that exploits the electrochemical reduction of oxygen, akin to the Clark electrode. To build the sensor, the transistor thin film fabrication protocol is integrated with the deposition of a gas permeable silicone membrane and a hydrogel electrolyte. To assess the sensor's power consumption, a model that links power consumption to the OECT geometry and the material properties of the semiconducting channel is established. This model identifies the optimized OECT design that is compatible with commercial near-field communication (NFC) microcontrollers. In the optimized design, the interrogating NFC radio signal is sufficient to power the microcontroller, achieve sensor readout, and transmit the digitized sensor current, enabling oxygen monitoring in air or water without wired connections or batteries. These findings provide a first example and quantitative argumentation on exploiting OECTs in low-power electrochemical sensor architectures.

1. Introduction

In the field of sensor technology, there is an increasing demand for wearable, portable, and point-of-care testing devices,[1,2] featuring wireless operation, efficient data reading, and low energy consumption.[3,4] In literature and on the market, prevalent wireless communication approaches rely on Bluetooth and WiFi protocols.[5–7] However, conventional batteries are still essential for powering these devices. An intriguing alternative lies in the integration of RFID (Radio Frequency IDentification) systems based on NFC (Near Field Communication) technology. This involves communication and powering through inductive coupling between the reader and tag coil antennas. These NFC-integrated circuits have been demonstrated to provide sufficient power for operating a wide range of microcontrollers and sensors, with the capability of storing data in the internal memory and accessing it through smartphone applications.[8–10] This approach has also been showcased in the advancing field of electrochemical sensing.[11–18] However, electrochemical sensors often provide only small current or voltage signals and rely on a three-electrode setup requiring feedback control. The necessary potentiostat circuit for their readout is difficult to implement with low-power integrated circuits and novel approaches to make electrochemical sensors compatible with NFC technology needed.

Among electrochemical sensors, there is significant interest in their application for gas monitoring and detection.[3,19] Specifically, research has concentrated on developing a wireless, wearable, and cost-effective oxygen sensor due to its relevance in healthcare,[20–22] food quality assessment,[17,19] microorganisms cultivation (i.e., microalga),[23,24] environmental monitoring, and personal safety devices.[3] In the latter field, oxygen deficiency detection is essential due to the profound consequences produced by slight changes in its concentration. Normal atmospheric oxygen concentration is 21%, with safe levels at 19.5% or above.[25,26] Below this level, asphyxiation symptoms can quickly take place: oxygen deficiencies may occur in enclosed spaces due to factors like storing organic materials[27,28] or displacing oxygen with other gases.[26,29] While fixed oxygen alarms are standard, portable monitors are essential for identifying low

L. G. D'Amico, C. Zhang, F. Decataldo, V. Vurro, M. Tessarolo, T. Cramer, B. Fraboni
Department of Physics and Astronomy
University of Bologna
Viale Carlo Berti Pichat 6/2, Bologna 40127, Italy
E-mail: tobias.cramer@unibo.it

C. Zhang
College of Materials Science and Engineering
Donghua University
Shanghai 201620, P. R. China

F. Decataldo
Department of Medical and Surgical Sciences
University of Bologna
Via Pelagio Palagi 9, Bologna 40138, Italy

I. Gualandi, F. Mariani, E. Scavetta
Department of Industrial Chemistry "Toso Montanari,"
University of Bologna
Via Piero Gobetti 85, Bologna 40129, Italy

The ORCID identification number(s) for the author(s) of this article can be found under https://doi.org/10.1002/admt.202401875

DOI: 10.1002/admt.202401875

oxygen levels in large facilities. Existing portable sensors are robust but face challenges in bulkiness and high cost,[30–32] hindering widespread adoption and integration into everyday work attire. Oxygen plays a crucial role at the microscopic scale, driving essential biological processes such as cell proliferation, bacterial defence, and tissue healing.[21] As a site-specific delivery and monitoring system is currently lacking,[22] the emerging field of smart wound dressings and monitoring, based on conductive biomaterials and hydrogels, is rapidly advancing. This field aims to create real-time, noninvasive, and portable healthcare devices with high precision and accuracy,[33–35] thereby expanding the demand for reliable wireless oxygen sensors.

Organic electrochemical transistors (OECTs) have gained significant attention in the field of electrochemical sensing and bioelectronics due to their low-voltage operation combined with large transconductances exceeding the amplification performance of common transistors.[36,37] Moreover, as OECTs rely on conjugated polymers as active materials, they are compatible with several solution-process deposition techniques allowing fabrication of flexible, stretchable, and low-cost devices that can be easily scaled up to industrial production.[38,39] In OECTs, the organic semiconducting channel and the gate electrode are connected through an electrolyte.[40–42] Controlling the bias applied to the gate terminal concerning the channel enables tuning the channel conductivity by electrochemical doping of the semiconducting polymer. The mixed ionic and electronic conductivity of the conjugated polymer channel assures that already small gate voltage changes cause significant variation in channel current. In electrochemical sensors, this amplification effect is exploited in different modalities.[43] The basic approach is to introduce a functionalized interface in the channel/electrolyte/gate system that produces a Nernstian voltage offset in function of the analyte concentration.[44–46] Possible interfaces to realize such potentiometric sensors are the channel/electrolyte interface,[47] the gate/electrolyte interface,[48,49] or a semipermeable membrane separating the gate and channel electrolyte.[50]

The most used conjugated polymer for OECTs is Poly(3,4-ethylenedioxythiophene) mixed with polystyrene sulfonate (PEDOT:PSS) due to its excellent electrical conductivity (>10^3 S cm^{-1}), high ionic conductivity, high electrochemical stability in its oxidized/doped form, and underwater stability.[51–53] Moreover, PEDOT:PSS is fully compatible with flexible and biodegradable substrates, wearable,[4] and textile technologies.[54–56] PEDOT:PSS-based OECTs have been developed for various biological sensing applications,[40,57–59] such as ascorbic acid,[60] dopamine,[61] uric acid,[56] vitamin A,[62] and single-cell detection,[63] all taking advantage of the high transconductance and amplification properties.

PEDOT:PSS is also suitable for OECT-based oxygen sensors as oxygen molecules oxidize PEDOT:PSS without external dopants or specific functionalization, enhancing the conductivity of the semiconducting channel.[64] The proposed kinetically favorable reaction is: $PEDOT^0+O_2+2H^+ \rightleftarrows PEDOT^{2+}+H_2O_2$.[65] Therefore, in the presence of solvated oxygen molecules in the electrolyte, the channel shows a higher conductivity and a larger potential needs to be applied to de-dope the channel. Recent works reporting this sensing principle have demonstrated PEDOT:PSS-based OECT oxygen sensors[66–68] reaching very low detection limits (0.07% of oxygen partial pressure in solution), elevated signal-to-noise ratio, and large I_{ds} percentage variation.[67] However, their application in gaseous environments is limited by the need for a liquid electrolyte. Solid hydrogel-gated OECTs provide a solution[68–70] allowing reliable and highly sensitive oxygen detection in the 13–21% concentration range."[68–70] An additional problematic issue of such OECT sensors regards their interference with other redox species when oxygen is measured in aqueous solutions.

In this work, we present the optimization of an OECT-based oxygen sensor toward energetic efficiency and sensor stability. In analogy to the Clark-electrode for oxygen sensing, we integrate the PEDOT:PSS based OECT with an oxygen-permeable membrane that prevents evaporation of the hydrogel electrolyte. The membrane also shields from interferences with other redox species potentially present when the oxygen content of aqueous media such as biological solutions is measured. To guide the design of an energetically efficient OECT sensor, we develop a simple analytical model that relates the power consumption to the precision of the sensor. The model reproduces the experimental data and demonstrates the critical role of the OECT channel geometry, PEDOT:PSS mixed ionic-electronic conductor properties, and electrolyte conductivity. By adapting the OECT design to these findings, we achieve an oxygen sensor that can be directly interfaced with a battery-less NFC microchip and antenna. The resulting fully passive device enables oxygen monitoring with a wireless readout in air and aqueous environments.

2. Results and Discussion

The structure of the oxygen sensor device developed for this study is reported in **Figure 1a**. It consists of an organic electrochemical transistor (OECT) patterned on a PEN thin film substrate. The OECT contains gold source, drain, and gate electrodes that are encapsulated by a Mr-DWL5 negative photoresist coating to prevent electrochemical reactions on the gold surface. The transistor channel and gate electrode are made of a thin film of poly(3,4-ethylenedioxythiophene) polystyrene sulfonate (PEDOT:PSS) with a thickness of 150 V. The gate and channel are both in contact with a hydrogel layer made of 1% w/v agarose in 0.1 M phosphate-buffered saline (PBS). The sensor is fully encapsulated by a silicone membrane (polydimethylsiloxane – PDMS) to achieve the selective detection of oxygen and to avoid hydrogel dehydration. Similar to a Clark electrode, the silicone membrane is permeable to oxygen molecules;[71,72] and therefore, an equilibrium of oxygen partial pressure is established between the hydrogel and the working environment. The oxygen sensing process then relies on electron transfer from the PEDOT:PSS to the oxygen. As a consequence of electron transfer, hole carriers are generated in the PEDOT phase (Figure 1a), causing an increase in transistor current. The reduced oxygen is subsequently transformed into hydrogen peroxide.[65]

The device and the fabrication process of the sensor are depicted in Figures 1b,c, respectively. The gold electrodes, the electrode encapsulation, and the PEDOT:PSS channel are patterned through photolithography on the PEN substrate. Then, the agarose hydrogel (thickness of 500 μm) is laminated on the active area, covering the gate and the channel, and encapsulated by a thin PDMS membrane. The PDMS membrane is fabricated on a PEN carrier substrate covered with PAA as a water-soluble

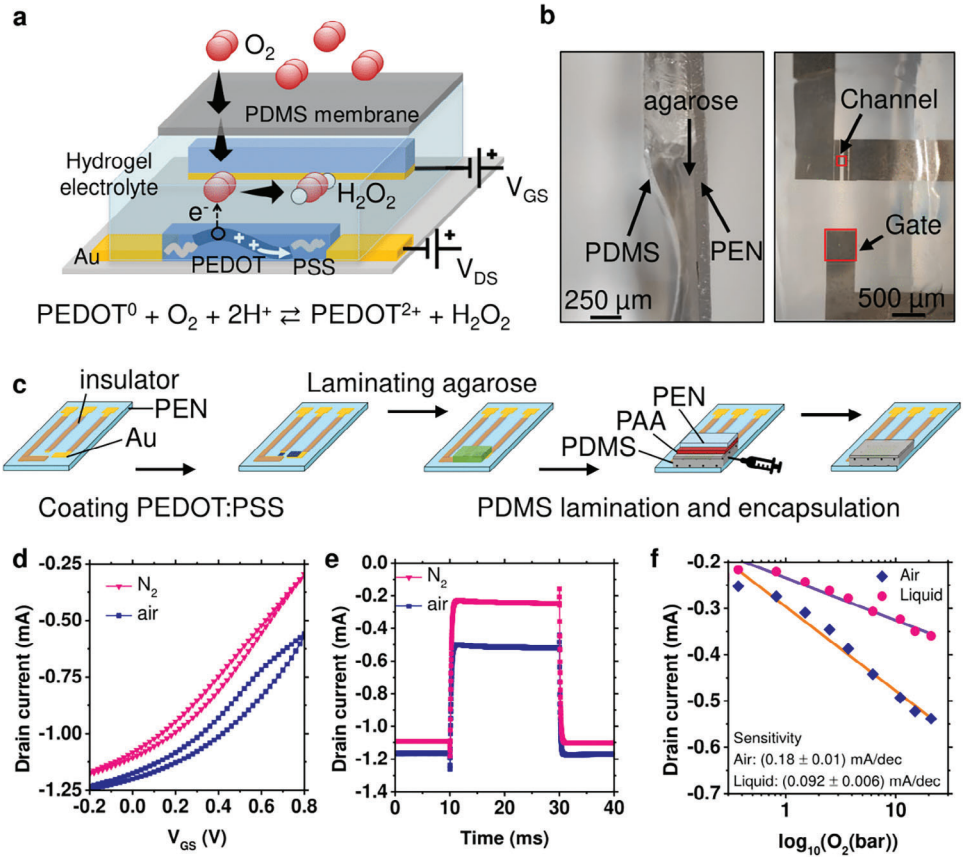

Figure 1. Organic electrochemical transistor (OECT) enabled oxygen sensor. a) Scheme of the device and sensing mechanism: oxygen diffuses through the PDMS membrane and the hydrogel to oxidize PEDOT, increasing the channel current. b) Optical images of the fabricated OECT sensor showing the cross-section through the layer stacks (left) and the micrometric channel and gate layout (right). c) Fabrication process of the encapsulated OECT. d) Transfer characteristics and e) transient response of the OECT as measured in pure nitrogen and air. f) Sensor current as a function of oxygen partial pressure measured in air (diamonds) or in 0.1 M KCl liquid solution (circles); a linear fit is performed on the experimental data obtaining a sensitivity of (0.18 ± 0.01) mA dec^{-1} (R^2 = 0.988, orange line) and of (0.092 ± 0.006) mA dec^{-1} (R^2 = 0.985, purple line).

sacrificial layer. Pictures of the final device (Figure 1b) illustrate the cross-section through the layer stacks as well as the micrometric channel and gate layout. A thicker hydrogel and encapsulation layer are observed at the borders of the device, but on top of the channel, we obtain a 30 µm-thick PDMS membrane and a 500 µm thick agarose hydrogel layer. Figure 1d shows the electrical transfer characteristics of the OECT recorded in the absence (100% N_2 atmosphere) and in the presence of oxygen (21%, air). In the presence of oxygen, the magnitude of the drain current increases as the channel oxidation causes a higher amount of hole carriers. The effect is present at all gate voltages but more pronounced at positive gate voltages, making it the most effective gate bias setting for oxygen sensing (V_G = 0.8 V). In this operating range, the device exhibits the lowest current, and the distinction between air and nitrogen environments is most pronounced, assuring a higher sensitivity to the oxygen variation. A second relevant sensor criterium is the transient response as investigated in Figure 1e. The drain current adapts within 0.2 ms to gate bias pulses with $V_{G,OFF}$ = 0 V and $V_{G,ON}$ = 0.8 V, demonstrating the fast device responses in both air and nitrogen. To quantify the device's sensitivity to oxygen, we operate the sensor in environments with controlled oxygen partial pressure. As environments, we use nitrogen atmosphere or saline aqueous solution (0.1 M KCl) both enriched with controlled amounts of oxygen. Sensor currents are measured during short bias pulses (V_G = 0.8 V, V_D = −0.3 V for 20 ms), keeping the sensor at ground bias for most of the time. This approach not only reduces energy consumption, as needed in realistic batteryless applications, but also ensures that calibration and measurement data are extracted under conditions that minimize device drift and hysteresis, as demonstrated in Figure S1, Supporting Information. Figure 1f shows the obtained calibration plots. The OECT output current linearly correlates with the logarithm of oxygen partial pressure, following the Nernst equation for potentiometric sensing. The device sensitivity for oxygen detection in water amounts to 0.17 ± 0.03 mA dec^{-1} when averaged over devices fabricated in different batches (N = 3). For oxygen sensing in water solution, the sensitivity is smaller and we obtain 0.09 ± 0.02 mA dec^{-1}. Compared to previous studies utilizing a hydrogel electrolyte in OECT oxygen sensors, we achieve a significant improvement in oxygen sensitivity,[68] which is assigned to the larger transconductance of the OECT (1.25 mS) due to the micrometric channel dimensions. In addition, the implementation of the pulsed-measurement protocol minimizes DC bias stress and enhances the reliability of the current data.

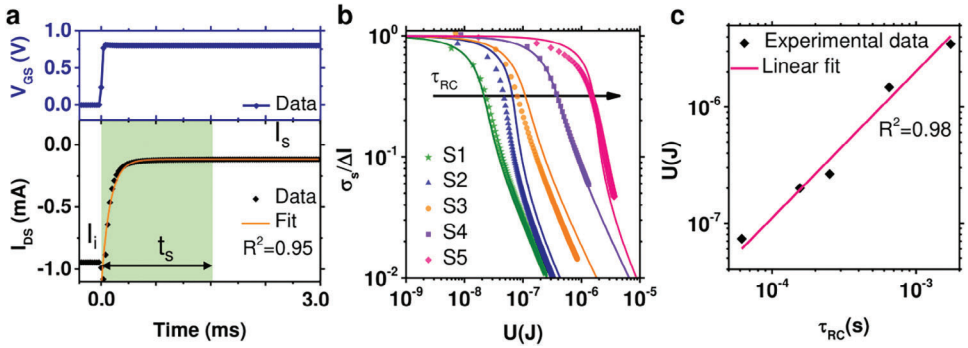

Figure 2. Energy consumption of a single OECT sensor readout. a) Typical transient response of an OECT when applying a bias pulse to the gate electrode at $t = 0$ s (the x-axis is shared). The sampling time t_S determines the sampling error σ_S, defined as the difference between the turn-off current I_S and the measured one I_{DS}. Equation (1) is employed to fit the experimental data (orange line), resulting in the extraction of the time constant $\tau_{RC} = (78 \pm 3)$ µs ($R^2 = 0.95$). b) Error of the measurement $\sigma_S/\Delta I$ as a function of the consumed energy for OECT devices having different time constants (S1: 60 µs, S2: 160 µs, S3: 251 µs, S4: 650 µs, S5: 1.70 ms). The experimental data points (markers) are fitted to the theoretical model (solid lines). c) Plot of energy needed for a single sensor readout with $\sigma_S/\Delta I = 5\%$ as a function of the OECT time constant. The red line shows a linear fit to the experimental data.

2.1. Model for the OECT Energy Consumption

Intending to achieve passive sensor operation, we investigate in detail the energy consumption of the OECT sensor. In our approach, we establish a relation between the consumed energy and the precision of a single sensor reading. More precise readings require longer averaging times; and hence, increase energy consumption. A sensor geometry, where the same reading precision is possible at shorter times would be energetically efficient. Hence, a model that provides the relation between energy consumption and sensor precision should provide details on how sensor geometry and semiconductor materials properties impact sensor efficiency. To derive such a relation, we consider the typical OECT transient drain current as measured during a sensor readout. Such a readout consists of switching the drain and gate potential from ground to defined values (here $V_G = 0.8$ V and $V_D = -0.3$ V); while, measuring the current for a sampling time t_s. **Figure 2a** shows that the measured drain current transient is well-described by the formula:[73]

$$I_D(t) = I_s + \Delta I e^{-t/\tau_{RC}} \tag{1}$$

in which τ_{RC} denotes the characteristic time constant defined by the capacitance C of the channel and the resistance R describing the ionic transport between the channel and the gate electrode.[74–76] Upon long measurement times, the current settles on the value I_S. The change in current due to the application of the gate potential is defined by $\Delta I = I_s - I_i$, where I_i denotes the drain current at $V_G = 0$ V. To obtain a sensor readout, the analog drain current must be digitized. In the most basic readout scheme, a single digital number I_{mean} is produced that represents the average current measured during the sampling interval t_s:

$$I_{mean} = \overline{I_D}(t_s) = \frac{1}{t_s}\int_0^{t_s} I_D(t)\,dt \tag{2}$$

In a simple readout design, the sampling interval starts when bias is applied to the OECT sensor. For long sampling times ($t_{s>>}\tau_{RC}$), the digital reading is a precise representation of the sensor current I_s. For shorter sampling times; however, a systematic error $\sigma_s = |I_s - I_{mean}|$ is introduced. In addition, the analog current is affected by random noise composed of thermal noise, current shot noise, and amplifier noise. Similarly, by increasing the sampling time, the impact of the analog noise is reduced. For our sensor, the intrinsic noise contributions stay below 3.2×10^{-22} $A^2\ Hz^{-1}$ for short noise and below 1.7×10^{-17} $V^2\ Hz^{-1}$ for thermal noise (see the Supporting Information), respectively, and can be neglected with respect to the error σ_s associated to the finite measurement time. Combining Equations (1) and (2), we obtain:

$$\sigma_s(t_s) = \left| -\Delta I \cdot \frac{\tau_{RC}}{t_s}\left(1 - e^{-\frac{t_s}{\tau_{RC}}}\right)\right| \tag{3}$$

Next, we consider the energy U consumed in a single sensor readout. The most significant contribution comes from Joule heating occurring due to the current flow through the OECT channel. From the transient OECT current, we obtain:

$$U(t_s) = \int_0^{t_s} I_D(t)\,V_D dt = V_D\left[I_s t_S + \Delta I \tau_{RC}\left(1 - e^{-\frac{t_s}{\tau_{RC}}}\right)\right] \tag{4}$$

By combining Equations (3) and (4) (see Supporting Information), we can eliminate the parameter t_s and obtain a general expression describing the measurement error σ_s in an OECT sensor as a function of the consumed energy U. The full analytic expression contains the Lambert function and is reported in the Supporting Information. An approximate linearized solution is:

$$\sigma_s(U) \overset{t_s \gg \tau_{RC}}{\rightarrow} k \times \frac{I_s}{(U-k)}, \text{with } k = \Delta I \tau_{RC} V_D \tag{5}$$

Figure 2b shows experimental data on the measurement error σ_s as a function of the consumed energy for single sensor readouts obtained in devices with different OECT time constants τ_{RC}. For each device, we observe that higher reading energies (as obtained by longer measurement times) result in a smaller reading error. On the double logarithmic scale of the plot, the curves converge to a slope of −1 at high reading energies, characteristic of the reciprocal relation between σ_s and U, as predicted by Equation (5). Taking the full expression for σ_s (Supporting

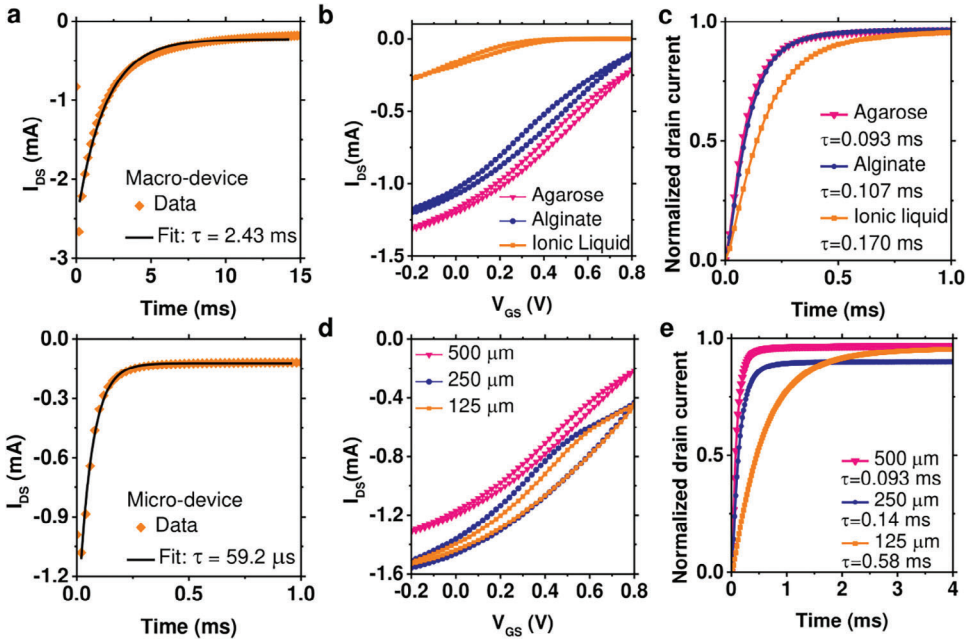

Figure 3. Optimization of the OECT sensor architecture. a) Comparison between the transient response of a macroscopic and microscopic OECT geometry in 0.1 M KCl liquid solution; the gate is switched at $t = 0$ from 0 to 0.8 V. b) Transfer characteristics and c) transient responses of devices with three distinct types of hydrogels, all with 500 µm thickness. d) Transfer characteristic and e) transient response of devices with three different thicknesses of the agarose hydrogel. All measurements are performed in air with a constant drain bias $V_{DS} = -0.3$ V. Equation (1) is used to fit the transient curves (a,c,e) with a resulting $R^2 = 0.99$.

Information), experimental data curves are well reproduced by the model also at lower reading energies.

These findings enable insight into how the sensor's energetic efficiency is determined by the OECT parameters. In slower OECTs with an increased time constant, longer measurement times are necessary to achieve a given readout precision. Accordingly, the error curve is shifted to higher energies for OECTs with larger time constants. To elaborate quantitatively on this concept, we determine for each OECT sensor the reading energy needed to keep the relative readout error $\sigma_s/\Delta I = 5\%$. Figure 2c shows the plot of the consumed energy as a function of the OECT time constant. The data follows over several orders of magnitude the linear relation given by Equation (5) and provides clear evidence for the importance of OECTs with a small time constant for energetic efficiency.

2.2. Geometry and Device Structure Optimization for Reduced Energy Consumption

Given the importance of the OECT time constant, we investigate how the sensor geometry and materials impact the transient response. The goal is to minimize the time constant to achieve an efficient sensor operation that is compatible with low-power, battery-less sensors, and wireless readout technologies. For OECTs, it is known that the transient response is dominated by the RC-time constant describing how ions migrate through the electrolyte with a resistance R to accumulate in the channel described by the capacitance C. Fast response is obtained by minimizing the resistance R as well as the capacitance C. **Figure** 3a compares the response of two OECT devices that differ in the channel geometry. Fast response with $\tau_{RC} = (59.2 \pm 1.2)$ µs is obtained in the devices with channel dimensions of $W = 100$ µm and $L = 50$ µm, here called micro-device. A much slower response with larger capacitive spikes emerges in the larger channel device (called macro-device) with $W = 2$ mm and $L = 2$ mm. For the macro device, a time constant of (2.43 ± 0.02) ms is extracted, making it energetically inefficient for sensor applications. The differences in time constant are directly related to the different channel areas and capacitances of the two devices.

Next, we consider the optimization of ion transport through the electrolyte to minimize the resistance R and achieve a fast OECT response. We test different electrolytes and electrolyte layer thicknesses, as reported in Figure 3 b–e. As electrolytes, we compare hydrogels of Agarose and Alginate, with a concentration of 1% w/v in 0.1 M PBS and 1.5% w/v in deionized water, respectively, to the ionic liquid 1-Ethyl-3-methylimidazolium ethyl sulfate as ionic conductor, keeping a fixed hydrogel thickness of 500 µm. The transfer characteristics (Figure 3b) as well as the drain current transients (Figure 3c) show that both hydrogels behave very similarly. Instead, the ionic liquid shows lower currents in the transfer curve with an overall smaller transconductance. Also, the transient obtained with the ionic liquid demonstrates a longer time constant attributed to a lower ionic conductivity with respect to the hydrogels. For the agarose hydrogel, we test different thicknesses of 125, 250, and 500 µm to evaluate its impact on the OECT response. The transfer characteristics show no significant dependence on hydrogel thickness, and the slope of the three compared curves is very similar. Only a smaller offset current is observed in the thicker hydrogel layer. Instead, the thickness has a significant impact on the transient response. The fastest

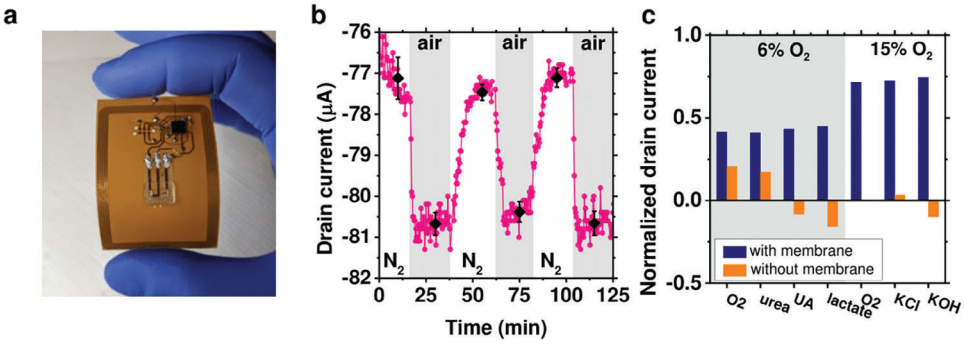

Figure 4. Batteryless NFC sensor application. a) Photo of the OECT-enabled sensor connected to an NFC microcontroller and antenna on a flexible printed circuit board. b) Real-time monitoring of the NFC sensor response during changes of the atmosphere from pure nitrogen (white background) to air (grey background). c) Oxygen sensing in water in the presence of competing redox-active or ionic analytes for membrane encapsulated (blue bars) and not encapsulated sensors (orange bars) for two oxygen concentrations, 6% and 15%. Values report the current variation with respect to the oxygen-free reference condition.

response is observed for the thicker agarose hydrogel layer. The increased thickness augments the cross section for ionic transport between the planar gate electrode and the channel as both are patterned on the same substrate below the hydrogel layer. This in turn reduces the resistance and the time constant of the device.

Following these results of the device structure optimization, we chose the micrometric OECT sensor with a 500 μm thick agarose hydrogel layer encapsulated by a 30 μm PDMS membrane for further integration and sensor tests. Previously reported devices demonstrated significantly higher power consumption, ranging from 35 to 110 μW.[67,68] In contrast, our newly optimized sensor achieved energy consumption below 100 nJ per sensing event, with a precision of 5%. This corresponded to a power consumption of less than 1 μW, marking a substantial improvement in energy efficiency. This achievement is entirely attributed to our structural optimization guided by the energy consumption model we developed.

2.3. Batteryless NFC Sensor Application

The optimized OECT oxygen sensor requires a current of ≈200 μA and 100 nJ for a single readout with 5% precision. Such specifications are compatible with wireless-powered NFC microcontrollers. The sensing mechanism with NFC involves the transmission of a radiofrequency signal from a cellphone to activate and interrogate the sensor device. The antenna absorbs the signal, and its energy is harvested to power the NFC microcontroller chip (here NXP NHS3152) and the OECT sensor. Then, the sensor readout signal is digitized and back-transmitted to the cell phone without the need to be powered by an additional energy source such as a battery. A batteryless sensor containing the antenna, the NFC chip, and the OECT oxygen sensor integrated on flexible plastic foil is shown in **Figure** 4a. The gate electrode is powered by a digital pin applying a constant positive voltage to the gate during readout. With these connections, the effective biases applied by the microcontroller during activation with the NFC radio signal are $V_{GS} \approx 0.8$ V and $V_{DS} \approx -0.05$ V.

To prove the correct reading of this fully passive oxygen sensor, we change repeatedly the sensors surrounding atmosphere, alternating pure nitrogen with air while monitoring the sensor signal. The data shown in Figure 4b demonstrate how the sensor monitors reliably the alterations in oxygen content. As expected, exposure to air reduces the OECT channel resistance as oxygen increases the amount of hole carriers in the semiconducting channel, causing a higher drain current. The NFC reading implies an error on the measurement equal to $\sigma_I = 2\%$ (error evaluation reported in Supporting Information), lower than the 5% previously evaluated as the maximum acceptable value.

To expand the usability of the sensor, we test it also for measuring the dissolved oxygen in an aqueous environment, aiming at validating its working and testing its reliability in the presence of potentially interfering redox active species. Due to the complexity of the media, the PEDOT:PSS channel can be oxidized or reduced by these interfering chemicals measuring dissolved oxygen, an extremely delicate process. In our sensor device, the PDMS membrane introduces a selective oxygen filter that is impermeable to other water-soluble agents. Notably, PDMS exhibits excellent gas permeability, enabling the efficient transfer of oxygen; while, simultaneously acting as a barrier against larger molecules.[71,77] To prove the selectivity of our sensor, we measure its response in artificial wound exudate, adding different interfering chemical compounds such as urea, UA, or lactate for which strong interference with PEDOT-based OECTs is observed.[54] For comparison, we repeat the same measurement in an OECT sensor that is in direct contact with the solution without hydrogel or PDMS membrane. Figure 4c reports the current deviation from the baseline acquired in pure nitrogen. At 6% O_2, we add urea (8.9 mM), uric acid (0.29 mM), and lactate (1.6 mM). At 15% O_2, we add KOH (8.4 mM) and KCl (0.18 M). For each addition, we monitor the device response for 15 min before adding the new chemical compound. Both 6% and 15% of oxygen concentration in the wound exudate produce the expected increase of the drain current for the membrane-protected sensor. In addition, the addition of the interfering chemicals does not alter the device response. This is even the case for stronger variations in ionic strength obtained by the addition of KCl or changes in pH due to KOH addition. Contrarily, it is demonstrated that without the membrane, it is not possible to get reliable sensor operation: the interference with the wound exudate causes a smaller current reduction at 15% O_2 than at 6%. Further, strong alterations occur when the interfering

substances are added or changes in ionic strength or pH occur. The findings demonstrate that the PDMS membrane enables selective oxygen sensing within a complex biological matrix, such as wound exudate, which contains various interfering oxidizing agents. In the absence of the protective membrane, the OECT sensor functionality is significantly compromised, as indicated by inconsistent current responses across varying oxygen concentrations and pronounced sensitivity to external factors such as interfering substances, fluctuations in ionic strength, and pH variations.

3. Conclusion

Our study demonstrates how a classical electrochemical sensor concept (i. e. the Clark electrode for oxygen sensing) can be translated into a fully passive sensor by exploiting the amplification introduced with organic electrochemical transistors (OECTs). For the case of oxygen sensing, we realize a PEDOT:PSS-based and hydrogel-gated OECT and show how such a thin film device can be integrated with a gas-permeable silicone membrane. Due to the membrane, the sensor shows stable operation without hydrogel degradation in air as well as in aqueous solutions and is shielded from interference with other redox-active analytes; while, maintaining a high sensitivity toward variations in oxygen partial pressure. We guide the sensor development with a quantitative model to evaluate OECT energy consumption. The analytical model describes how the energy consumed during sensor readout depends on the OECTs switching time constant τ and offset current I_s. Therefore, it informs on how typical OECT parameters such as the device geometry (channel dimensions, hydrogel thickness) or material properties (volumetric capacitance, hydrogel conductivity) have to be optimized to reduce power consumption. Following these findings, we realize an OECT with PEDOT:PSS as the semiconducting material that exhibits a small channel ($W = 100$ µm and $L = 50$ µm) and a 500 µm-thick agarose hydrogel as the electrolyte to achieve a fast device response (93.2 ± 0.8) µs and an energy consumption of less than 100 nJ for a sensor readout with 5% precision. This represents a significant improvement in energy efficiency compared to previously published articles, where devices exhibited minimum power consumption of 37[68] and 106 µW.[67] requiring readout times for a single reading > 100 ms. The optimized sensor is fully compatible with the power and current requirements of a commercial NFC chip to achieve a wireless and battery-free sensor. The resulting fully passive electrochemical sensor permits oxygen monitoring in ambient or aqueous solutions. With this work, we provide quantitative arguments on how organic electrochemical transistors can play a role in future low-power electrochemical sensor devices.

4. Experimental Section

OECT Fabrication: Polyethylene naphthalate (PEN) substrates (125 µm, GoodFellow) were cleaned and treated with oxygen plasma (50 W for 1 min, Tergeo Plus PIE Scientific). Microposit S1818 (Micro Resist Technology GmbH) positive photoresist was spin-coated onto the PEN substrate (4000 rpm for 60s) and annealed for 1 min at 110 °C. The photoresist was patterned through direct laser lithography. The metal contacts (7 nm chromium and 30 nm gold) were thermally evaporated. The lift-off was carried out immersing the samples in acetone for 4 h. Metal feedlines were encapsulated by mr-DWL5 negative photoresist (Micro Resist Technology GmbH), spin-coated (3000 rpm for 30 s), and annealed for 2 min at 100 °C. Photolithography was immediately followed by annealing for 2 min at 100 °C. After 1 h of cooling down, the negative photoresist was developed and plasma treated (120 W for 2 min). Then, they were baked by a temperature ramp (from room temperature up to 120 °C in 15 min) and left at the final temperature for 30 min. To pattern the PEDOT:PSS channel, a first layer of S1818 was spin-coated and annealed for 30 s at 110 °C; then, a second layer was spin-coated and annealed for 1 min followed by photolithography development and surface activation with plasma in air (15 W for 2 min). PEDOT:PSS solution (93.75% PEDOT:PSS Clevios PH1000) with 5% ethylene glycol (Sigma–Aldrich), 1% 3-glycidoxypropyltrimethoxysilane (GOPS) (Sigma–Aldrich), and 0.25% 4-dodecylbenzenesulfonicacid (DBSA) (Sigma–Aldrich) was kept in an ultrasonic bath for 10 min, filtered with 1.2 µm cellulose acetate filters (Sartorius), and spin-coated (3000 rpm for 9 s) on the patterned S1818 double layer. After annealing for 1 h at 120 °C, the devices were immersed in isopropanol for 4 h for lift-off (see Supporting Information). Devices with different channel and gate geometries were prepared as detailed in Table S1, Supporting Information. Transconductance of OECTs with $W = 100$ um and $L = 50$ um and PEDOT:PSS layer thickness of 150 nm had an average value of $g_m = 1.25 \pm 0.30$ mS when averaging over different fabrication batches ($N = 10$).

OECT Encapsulation: Agarose hydrogel was prepared with a solution of 1% w/v agarose (Sigma–Aldrich) in 0.1 M phosphate-buffered saline solution (pH 7.00). The solution was stirred for 40 min at 100° and then injected inside a mold of the desired thickness (125, 250, and 500 µm). After 4 h of solidification, the hydrogel was removed from the mold and stored in PBS. The OECT was soaked in deionized water overnight, and the hydrogel was cut and positioned on the OECT to cover the channel and the gate area. A second PEN substrate was coated with a solution of 10% v/v poly(acrylic acid) PAA in distilled water by spin coating (3000 rpm for 60 s). Then, a mixture of 10:1 PDMS:curing agent was spin-coated on top of the PAA layer (60 s, 2000 rpm for 30 µm or 4000 rpm for 6 µm thickness, respectively). The covered PEN sheet was kept at 70 °C for 1 h for PDMS solidification. The prepared PEN sheet was pressed against the OECT/hydrogel structure and with a syringe, additional PDMS mixture was injected to construct the sidewalls. Final PDMS solidification was achieved at 50 °C for 4 h. In the final step, the top PEN layer was released from the device by dissolving the sacrificial PAA layer in distilled water for 1 h. In addition to OECTs with agarose hydrogel, a photopolymerized ionic liquid gel and an alginate hydrogel were prepared. The ionic liquid gel was prepared by mixing 69.7% w/w 1-Ethyl-3-methylimidazolium ethyl sulfate (Sigma–Aldrich), 0.3% w/w 2-Hydroxy-2-methylpropiophenone (Sigma–Aldrich), and 30% w/w Poly(ethylene glycol) diacrylate (Sigma–Aldrich). The mixture was then injected inside a mold of the desired thickness and exposed to UV light using a Radium HRC 300-280 (Sanolux) for 1 min. The alginate hydrogel was obtained by direct injection of 300 µL of a 5% w/v $CaCl_2$ (Sigma–Aldrich) solution inside a mold of the desired thickness, which was then filled up with 1.5% w/v alginate (Sigma–Aldrich) solution.

Electrical Characterizations: The DC and transient characterizations were carried out with a source-measure unit (SMU, Keysight B2912A). For fully passive measurements, an NHS3152 integrated circuit (NXP Semiconductors) was connected to the three terminals of the OECT. The NFC chip was wired to the controller board, and custom software was uploaded onto the microprocessor (see Supporting Information). All wires were then removed, and upon activation by the NFC signal of a cellphone, the measurement chip performed OECT readout and data transfer to the cellphone without any additional power supply. The energy consumption of the sensor device was determined based on measured current and voltage transients. For oxygen sensing characterizations, the devices were inserted inside a glass vial with a polypropylene screw cap with Natural PTFE/Natural silicone septa cap. Outlet and inlet needles were inserted through the cap; the latter was connected to the flowmeter to control the flux of pure nitrogen, 5% oxygen mixture and pure oxygen. For measurements in liquid, the inlet needle and the OECT active area were immersed in the liquid, which filled up almost the whole vial volume (15 mL). Two liquids were employed to test the device: a solution of KCl 0.1 M in distilled water and

artificial wound exudate prepared as described in previous work.[54] Before starting to measure, the vial was firstly depleted from the air, fluxing only pure nitrogen for more than 30 min; then, the oxygen concentration was changed using the flowmeter. The interference test was carried out by injecting the chemical compounds into the liquid with a needle passing through the vial cap. Typical concentrations including potassium chloride KCl, urea, uric acid (UA), and lactate, were intentionally introduced in controlled amounts.[54,78] Furthermore, a pH variation was induced by adding a controlled amount of potassium hydroxide.

Supporting Information

Supporting Information is available from the Wiley Online Library or from the author.

Acknowledgements

L.G.D'A. and C.Z. contributed equally to this work. The authors acknowledge the help of the company Bioage-SRL in the development of the NFC flexible passive readout device. T.C. acknowledges financial support from the Space It Up project funded by the Italian Space Agency, ASI and the Ministry of University and Research, MUR, under contract n. 2024-5-E.0 – CUP n. I53D24000060005.

Open access publishing facilitated by Universita degli Studi di Bologna, as part of the Wiley - CRUI-CARE agreement.

Conflict of Interest

The authors declare no conflict of interest.

Data Availability Statement

The data that support the findings of this study are available from the corresponding author upon reasonable request.

Keywords

battery-less sensors, near field communication, organic electrochemical transistors, oxygen sensors, sensor energy efficiency

Received: November 6, 2024
Revised: January 13, 2025
Published online:

[1] D. C. Christodouleas, B. Kaur, P. Chorti, *ACS Cent. Sci.* **2018**, *4*, 1600.
[2] Q. Gao, S. Li, *Interdiscip. Med.* **2024**, *2*, e20230031.
[3] A. Bag, N.-E. Lee, *Adv. Mater. Technol.* **2021**, *6*, 2000883.
[4] Z. Lou, L. Wang, G. Shen, *Adv. Mater. Technol.* **2018**, *3*, 1800444.
[5] J. M. Stine, L. A. Beardslee, R. M. Sathyam, W. E. Bentley, R. Ghodssi, *Sens. Actuators, B* **2020**, *320*, 128381.
[6] S.-J. Choi, S.-J. Kim, I.-D. Kim, *NPG Asia Mater.* **2016**, *8*, e315.
[7] J. Park, J. Kim, K. Kim, S.-Y. Kim, W. H. Cheong, K. Park, J. H. Song, G. Namgoong, J. J. Kim, J. Heo, F. Bien, J.-U. Park, *Nanoscale* **2016**, *8*, 10591.
[8] Y. Cheng, K. Wang, H. Xu, T. Li, Q. Jin, D. Cui, *Anal. Bioanal. Chem.* **2021**, *413*, 6037.
[9] J. M. Azzarelli, K. A. Mirica, J. B. Ravnsbæk, T. M. Swager, *Proc. Natl. Acad. Sci. U. S. A.* **2014**, *111*, 18162.
[10] A. Lazaro, R. Villarino, M. Lazaro, N. Canellas, B. Prieto-Simon, D. Girbau, *Biosensors* **2023**, *13*, 775.
[11] L. Fiore, V. Mazzaracchio, A. Serani, G. Fabiani, L. Fabiani, G. Volpe, D. Moscone, G. M. Bianco, C. Occhiuzzi, G. Marrocco, F. Arduini, *Sens. Actuators, B* **2023**, *379*, 133258.
[12] J. Choi, I. Visagie, Y. Chen, R. Abbel, K. Parker, *Sensors* **2023**, *23*, 6765.
[13] H. Mirzajani, T. Abbasiasl, F. Mirlou, E. Istif, M. J. Bathaei, Ç. Dağ, O. Deyneli, D. Yazıcı, L. Beker, *Biosens. Bioelectron.* **2022**, *213*, 114450.
[14] Z. Ma, P. Chen, W. Cheng, K. Yan, L. Pan, Y. Shi, G. Yu, *Nano Lett.* **2018**, *18*, 4570.
[15] S. Shrivastava, T. Q. Trung, N.-E. Lee, *Chem. Soc. Rev.* **2020**, *49*, 1812.
[16] H. Li, H. Gong, T. H. Wong, J. Zhou, Y. Wang, L. Lin, Y. Dou, H. Jia, X. Huang, Z. Gao, R. Shi, Y. Huang, Z. Chen, W. Park, J. Y. Li, H. Chu, S. Jia, H. Wu, M. Wu, Y. Liu, D. Li, J. Li, G. Xu, T. Chang, B. Zhang, Y. Gao, J. Su, H. Bai, J. Hu, C. K. Yiu, et al., *Nat. Commun.* **2023**, *14*, 7539.
[17] R. Zhu, M. Desroches, B. Yoon, T. M. Swager, *ACS Sens.* **2017**, *2*, 1044.
[18] P. Escobedo, M. M. Erenas, N. López-Ruiz, M. A. Carvajal, S. Gonzalez-Chocano, I. de Orbe-Payá, L. F. Capitán-Valley, A. J. Palma, A. Martínez-Olmos, *Anal. Chem.* **2017**, *89*, 1697.
[19] G. Barandun, L. Gonzalez-Macia, H. S. Lee, C. Dincer, F. Güder, *ACS Sens.* **2022**, *7*, 2804.
[20] S.-H. Lu, M. Samandari, C. Li, H. Li, D. Song, Y. Zhang, A. Tamayol, X. Wang, *Sens. Actuators Rep.* **2022**, *4*, 100075.
[21] S. Schreml, R. M. Szeimies, L. Prantl, S. Karrer, M. Landthaler, P. Babilas, *Br. J. Dermatol.* **2010**, *163*, 257.
[22] M. Ochoa, R. Rahimi, J. Zhou, H. Jiang, C. K. Yoon, D. Maddipatla, B. B. Narakathu, V. Jain, M. M. Oscai, T. J. Morken, R. H. Oliveira, G. L. Campana, O. W. Cummings, M. A. Zieger, R. Sood, M. Z. Atashbar, B. Ziaie, *Microsyst. Nanoeng.* **2020**, *6*, 46.
[23] F. Abiusi, R. H. Wijffels, M. Janssen, *ACS Sustainable Chem. Eng.* **2020**, *8*, 6065.
[24] A. Kazbar, G. Cogne, B. Urbain, H. Marec, B. Le-Gouic, J. Tallec, H. Takache, A. Ismail, J. Pruvost, *Algal Res.* **2019**, *39*, 101432.
[25] U. Svedberg, J. Samuelsson, S. Melin, *Ann. Occup. Hyg.* **2008**, *52*, 259.
[26] T. J. Peterson, J. G. Weisend II, J. Jurns, S. Woods, *Oxygen Deficiency Hazards. In: Cryogenic Safety. International Cryogenics Monograph Series.*, Springer, Cham, Switzerland AG **2019**.
[27] J. C. Devitt, M. K. D. Hall, A. J. Najar-Rodriguez, J. R. Beggs, *J. Stored Prod. Res.* **2020**, *88*, 101670.
[28] D. Ochandio, R. Bartosik, A. Gastón, R. Abalone, A. A. Barreto, A. Yommi, *J. Stored Prod. Res.* **2017**, *74*, 36.
[29] T. Watanabe, M. Morita, *Forensic Sci. Int.* **1998**, *96*, 47.
[30] "*GASTECH Portable Gas Detectors – Single Gas Detectors*", https://gastech.com/products/gas-detectors-portable/single-gas (accessed: 30 January 2025).
[31] "*O2 Microsensor for Research Applications*", *Unisense*, https://unisense.com/products/o2-microsensor/ (accessed: January 2025).
[32] *GaslabCom*, https://gaslab.com/collections/oxygen (accessed: January 2025).
[33] L. Wang, M. Zhou, T. Xu, X. Zhang, *Chem. Eng. J.* **2022**, *433*, 134625.
[34] R. Yu, H. Zhang, B. Guo, *Nano-Micro Lett.* **2021**, *14*, 1.
[35] M. Serafini, F. Mariani, I. Gualandi, F. Decataldo, L. Possanzini, M. Tessarolo, B. Fraboni, D. Tonelli, E. Scavetta, *Sensors* **2021**, *21*, 7905.
[36] M. Sophocleous, L. Contat-Rodrigo, E. García-Breijo, J. Georgiou, *IEEE Sens. J.* **2021**, *21*, 3977.
[37] M. Sessolo, J. Rivnay, E. Bandiello, G. G. Malliaras, H. J. Bolink, *Adv. Mater.* **2014**, *26*, 4803.
[38] M. Zabihipour, R. Lassnig, J. Strandberg, M. Berggren, S. Fabiano, I. Engquist, P. A. Ersman, *npj Flexible Electron.* **2020**, *4*, 15.
[39] A. Marks, S. Griggs, N. Gasparini, M. Moser, *Adv. Mater. Interfaces* **2022**, *9*, 2102039.
[40] J. Rivnay, S. Inal, A. Salleo, R. M. Owens, M. Berggren, G. G. Malliaras, *Nat. Rev. Mater.* **2018**, *3*, 17086.

[41] A. Makhinia, L. Bynens, A. Goossens, J. Deckers, L. Lutsen, K. Vandewal, W. Maes, V. Beni, P. A. Ersman, *Adv. Funct. Mater.* **2024**, *34*, 2314857.
[42] Y. Zhong, N. Lopez-Larrea, M. Alvarez-Tirado, N. Casado, A. Koklu, A. Marks, M. Moser, I. McCulloch, D. Mecerreyes, S. Inal, *Chem. Mater.* **2024**, *36*, 1841.
[43] F. Torricelli, D. Z. Adrahtas, Z. Bao, M. Berggren, F. Biscarini, A. Bonfiglio, C. A. Bortolotti, C. D. Frisbie, E. Macchia, G. G. Malliaras, I. McCulloch, M. Moser, T.-Q. Nguyen, R. M. Owens, A. Salleo, A. Spanu, L. Torsi, *Nat. Rev. Methods Primers* **2021**, *1*, 66.
[44] T. Cramer, A. Campana, F. Leonardi, S. Casalini, A. Kyndiah, M. Murgia, F. Biscarini, *J. Mater. Chem. B* **2013**, *1*, 3728.
[45] I. Gualandi, M. Tessarolo, F. Mariani, T. Cramer, D. Tonelli, E. Scavetta, B. Fraboni, *Sens. Actuators, B* **2018**, *273*, 834.
[46] B. Burtscher, C. Diacci, A. Makhinia, M. Savvakis, E. O. Gabrielsson, L. Veith, X. Liu, X. Strakosas, D. T. Simon, *npj Biosensing* **2024**, *1*, 7.
[47] A. M. Pappa, D. Ohayon, A. Giovannitti, I. P. Maria, A. Savva, I. Uguz, J. Rivnay, I. McCulloch, R. M. Owens, S. Inal, *Sci. Adv.* **2018**, *4*, eaat0911.
[48] S. Casalini, A. C. Dumitru, F. Leonardi, C. A. Bortolotti, E. T. Herruzo, A. Campana, R. F. De Oliveira, T. Cramer, R. Garcia, F. Biscarini, *ACS Nano* **2015**, *9*, 5051.
[49] A. Moudgil, K. Hou, T. Li, W. L. Leong, *Adv. Mater. Technol.* **2023**, *8*, 2300605.
[50] D. A. Koutsouras, K. Lieberth, F. Torricelli, P. Gkoupidenis, P. W. M. Blom, *Adv. Mater. Technol.* **2021**, *6*, 2100591.
[51] A.-M. Pappa, O. Parlak, G. Scheiblin, P. Mailley, A. Salleo, R. M. Owens, *Trends Biotechnol.* **2018**, *36*, 45.
[52] S.-M. Kim, N. Kim, Y. Kim, M.-S. Baik, M. Yoo, D. Kim, W.-J. Lee, D.-H. Kang, S. Kim, K. Lee, M.-H. Yoon, *NPG Asia Mater.* **2018**, *10*, 255.
[53] S. Zhang, E. Hubis, C. Girard, P. Kumar, J. DeFranco, F. Cicoira, *J. Mater. Chem. C* **2016**, *4*, 1382.
[54] F. Mariani, M. Serafini, I. Gualandi, D. Arcangeli, F. Decataldo, L. Possanzini, M. Tessarolo, D. Tonelli, B. Fraboni, E. Scavetta, *ACS Sens.* **2021**, *6*, 2366.
[55] L. Possanzini, F. Decataldo, F. Mariani, I. Gualandi, M. Tessarolo, E. Scavetta, B. Fraboni, *Sci. Rep.* **2020**, *10*, 17180.
[56] D. Arcangeli, I. Gualandi, F. Mariani, M. Tessarolo, F. Ceccardi, F. Decataldo, F. Melandri, D. Tonelli, B. Fraboni, E. Scavetta, *ACS Sens.* **2023**, *8*, 1593.
[57] H.-S. Tseng, Y.-L. Chen, P.-Y. Zhang, Y.-S. Hsiao, *ACS Appl. Mater. Interfaces* **2024**, *16*, 25601.
[58] G. E. Fenoy, R. Hasler, C. Lorenz, J. Movilli, W. A. Marmisollé, O. Azzaroni, J. Huskens, P. Bäuerle, W. Knoll, *ACS Appl. Mater. Interfaces* **2023**, *15*, 10885.
[59] J. Song, H. Liu, Z. Zhao, P. Lin, F. Yan, *Adv. Mater.* **2023**, *36*, 2300034.
[60] I. Gualandi, E. Scavetta, F. Mariani, D. Tonelli, M. Tessarolo, B. Fraboni, *Electrochim. Acta* **2018**, *268*, 476.
[61] I. Gualandi, D. Tonelli, F. Mariani, E. Scavetta, M. Marzocchi, B. Fraboni, *Sci. Rep.* **2016**, *6*, 35419.
[62] L. Salvigni, F. Mariani, I. Gualandi, F. Decataldo, M. Tessarolo, D. Tonelli, B. Fraboni, E. Scavetta, *Sens. Actuators, B* **2023**, *393*, 134313.
[63] F. Bonafè, F. Decataldo, I. Zironi, D. Remondini, T. Cramer, B. Fraboni, *Nat. Commun.* **2022**, *13*, 5423.
[64] J. Ehlich, L. Migliaccio, I. Sahalianov, M. Nikić, J. Brodský, I. Gablech, X. T. Vu, S. Ingebrandt, E. D. Głowacki, *J. Neural Eng.* **2022**, *19*, 036045.
[65] A. Giovannitti, R. B. Rashid, Q. Thiburce, B. D. Paulsen, C. Cendra, K. Thorley, D. Moia, J. T. Mefford, D. Hanifi, D. Weiyuan, M. Moser, A. Salleo, J. Nelson, I. McCulloch, J. Rivnay, *Adv. Mater.* **2020**, *32*, 1908047.
[66] S.-E. Wu, L. Yao, A. Shiller, A. H. Barnard, J. D. Azoulay, T. N. Ng, *Adv. Electron. Mater.* **2021**, *7*, 2100223.
[67] F. Decataldo, I. Gualandi, M. Tessarolo, E. Scavetta, B. Fraboni, *APL Mater.* **2020**, *8*, 091103.
[68] F. Decataldo, F. Bonafè, F. Mariani, M. Serafini, M. Tessarolo, I. Gualandi, E. Scavetta, B. Fraboni, *Polymers* **2022**, *14*, 1022.
[69] C.-H. Kim, M. Azimi, J. Fan, H. Nagarajan, M. Wang, F. Cicoira, *Nanoscale* **2023**, *15*, 3263.
[70] X. Wu, S. Chen, M. Moser, A. Moudgil, S. Griggs, A. Marks, T. Li, I. McCulloch, W. L. Leong, *Adv. Funct. Mater.* **2023**, *33*, 2209354.
[71] D. A. Markov, E. M. Lillie, S. P. Garbett, L. J. McCawley, *Biomed. Microdevices* **2014**, *16*, 91.
[72] A. Mata, A. J. Fleischman, S. Roy, *Biomed. Microdevices* **2005**, *7*, 281.
[73] D. A. Bernards, G. G. Malliaras, *Adv. Funct. Mater.* **2007**, *17*, 3538.
[74] J. Rivnay, P. Leleux, M. Ferro, M. Sessolo, A. Williamson, D. A. Koutsouras, D. Khodagholy, M. Ramuz, X. Strakosas, R. M. Owens, C. Benar, J.-M. Badier, C. Bernard, G. G. Malliaras, *Sci. Adv.* **2015**, *1*, e1400251.
[75] C. M. Proctor, J. Rivnay, G. G. Malliaras, *J. Polym. Sci., Part B: Polym. Phys.* **2016**, *54*, 1433.
[76] M. Bianchi, S. Carli, M. Di Lauro, M. Prato, M. Murgia, L. Fadiga, F. Biscarini, *J. Mater. Chem. C* **2020**, *8*, 11252.
[77] E. A. Grushevenko, I. L. Borisov, A. V. Volkov, *Pet. Chem.* **2021**, *61*, 959.
[78] N. J. Trengove, S. R. Langton, M. C. Stacey, *Wound Repair Regener.* **1996**, *4*, 234.